Applied Catalysis B: Environmental 186 (2016) 193–203

Contents lists available at ScienceDirect

Applied Catalysis B: Environmental

journal homepage: www.elsevier.com/locate/apcatb

# Superior performance of 3 D Co-Ni bimetallic oxides for catalytic degradation of organic dye: Investigation on the effect of catalyst morphology and catalytic mechanism

Xueyan Liu [a], Dan Xu [a], Danfeng Zhang [a,b], Guozhen Zhang [a], Lei Zhang [a,*]

[a] College of Chemistry, Liaoning University, Shenyang 110036, China
[b] College of Sciences, Heilongjiang Bayi Agricultural University, Heilongjiang 163319, China

ARTICLE INFO

*Article history:*
Received 23 October 2015
Received in revised form 4 December 2015
Accepted 6 January 2016
Available online 12 January 2016

*Keywords:*
3D hierarchical dandelion-like $NiCo_2O_4$ spheres
Degradation
Microwave irradiation
Congo red

ABSTRACT

An application of novel magnetic separable $NiCo_2O_4$ in microwave-induced catalytic degradation (MICD) of organic dye was found, and the structures of $NiCo_2O_4$ significantly affect its catalytic activity. Diverse $NiCo_2O_4$ structures, including $NiCo_2O_4$ nanoplates ($NiCo_2O_4$-P), $NiCo_2O_4$ nanorods ($NiCo_2O_4$-R), $NiCo_2O_4$ nanoparticles ($NiCo_2O_4$-N) and three-dimensional (3D) hierarchical dandelion-like $NiCo_2O_4$ spheres (3D $NiCo_2O_4$-S), have been successfully synthesized. Among them, 3D $NiCo_2O_4$-S displayed superior catalytic activity for congo red (CR) under microwave (MW) irradiation. Enhanced catalytic activity of 3D $NiCo_2O_4$-S can be attributed to the higher MW energy harvesting capacity resulted from multiple absorption of MW and relatively high specific surface area. Various scavengers, the band structure, as well as Mott–Schottky analysis, were utilized to identify the roles of active species. A possible catalytic mechanism was proposed. The 3D $NiCo_2O_4$-S is expected to have potential applications in pollutants degradation because of its efficient catalysis, easy separation and good reusability.



## 1. Introduction

Water pollution is an increasing serious challenge for the whole world. Being one of the important pollutants, dyes have caused great concerns for harmful impacts on human health and the environment due to their toxicity, non-biodegradability and potential carcinogenicity. Several methods such as flocculation [1], precipitation [2], ion-exchange [3], photodegradation [4,5], adsorption [6,7], chemical oxidation [8], MICD [9] and even microbiological treatment [10], have been developed for dyes removal. Among them, MICD process, especially coupled with some appropriate MW absorbents as catalysts [11–13], is considered as a promising technology for its short reaction time, low activation energy, and high reaction rate.

Over the past decades, activated carbon [14,15], polymers [16] and metal oxides [17,18] were commonly used in MICD of organic contaminants. Recently, bimetal oxides have also attracted considerable attention due to their excellent catalytic properties as well as magnetic properties. As the typical bimetal oxides, ferrites referred as $MeFe_2O_4$ (Me = Mg, Cu, Co, Ni and Cd etc.), appeared to be particularly efficient just as our previous researches found [19].

But now, we are interested in exploring another bimetal oxide, magnetic $NiCo_2O_4$, because of its intriguing advantages such as low cost, high stability, relatively abundance, environmental friendliness [20], excellent microwave absorption performance [21], controllable size and shape. It is well known that the size and morphology of material can strongly influence its catalytic properties. Thus, morphology controlled synthesis becomes an important issue. To date, spinel $NiCo_2O_4$ with diverse morphologies such as nanoplates [22], mesoporous structures [23], nanoparticles [24], nanorod [25], nanoneedles [26] and nanowires [27] and so on, have been reported and widely used in supercapacitors [28], electrochemical sensors [29], drug delivery [30] and Li-ion batteries [31]. Although there are many reports about the applications of $NiCo_2O_4$, to our knowledge, the investigation about its application in MICD is rare.

In this work, we prepared 3D $NiCo_2O_4$-S by a facile solvothermal-calcination method. For comparison, $NiCo_2O_4$-R, $NiCo_2O_4$-P and $NiCo_2O_4$-N were also synthesized. CR was employed as target pollutants to evaluate microwave-induced catalytic performance of the materials. The focuses were on the following respects: (1) exploring potential application of $NiCo_2O_4$ in MICD for dye; (2) discussing the relationship between the enhanced MW

* Corresponding author. Tel.: +86 024 62202380; Fax: +86 024 62202380.
*E-mail address:* zhanglei63@126.com (L. Zhang).

http://dx.doi.org/10.1016/j.apcatb.2016.01.005
0926-3373/

catalytic activity of $NiCo_2O_4$ and their morphologies; (3) inspecting the intermediate and final degradation products via UV–vis, HPLC and ionic chromatography (IC); (4) identifying the types of active species by adding several scavengers; (5) inferring the mechanism for the enhanced catalytic activity based on the types of active species and the separation process of electron/hole pairs.

## 2. Experimental

### 2.1. Chemicals

CR ($C_{32}H_{22}N_6Na_2O_6S_2$), $NiSO_4{\cdot}7H_2O$, $CoCl_2{\cdot}6H_2O$, $Ni(CH_3COO)_2{\cdot}4H_2O$, $Co(CH_3COO)_2{\cdot}4H_2O$, urea, ethylene glycol, hexadecyl trimethyl ammonium bromide (CTMAB), sodium acetate (NaAc), tetra-butyl ammonium bromide (TBAB), *tert*-butyl alcohol (TBA), ethylene diaminetetra acetic acid disodium salt (EDTA-2Na), bicarbonate ($NaHCO_3$), sodium oxalate ($Na_2C_2O_4$), terephthalic acid (TA) were obtained from Sinopharm Chemical Reagent Co., Ltd. (Shenyang, China) and used directly as received.

### 2.2. Synthesis of various magnetic $NiCo_2O_4$ catalysts

The 3D $NiCo_2O_4$-S precursor was prepared by a facile solvothermal method. In a typical process, 0.4213 g of $NiSO_4{\cdot}7H_2O$ and 0.7138 g of $CoCl_2{\cdot}6H_2O$ were completely dissolved in 30 mL pure water under constant magnetic stirring, followed by the addition of 0.8108 g urea. After mixing for 30 min, the transparent solution was poured into a Teflon-lined autoclave (100 mL) at 180 °C for 6.5 h. After the mixture was cooled to room temperature, the product was collected magnetically and washed with water. Then, the obtained pink $NiCo_2O_4$ precursor was dried at 60 °C in an oven overnight. Lastly, the precursor was calcined at 400 °C in air atmosphere for 3 h with a ramping rate of 2 °C $min^{-1}$ to obtain the black $NiCo_2O_4$ powder.

For comparison, other three different morphology of $NiCo_2O_4$ were prepared as follows.

$NiCo_2O_4$-P precursor was synthesized by a hydrothermal method according to a previous report [32]. Typically, 0.2488 g $Ni(CH_3COO)_2{\cdot}4H_2O$, 0.4759 g $CoCl_2{\cdot}6H_2O$ and 0.1 g CTMAB were dissolved in 40 mL deionized water with continuous stirring for 60 min. Then, 3.2 g NaOH was added to this solution and stirred for 10 min. The solution was then hydrothermally reacted at 160 °C for 20 h. Then, the product was dried at 60 °C overnight.

$NiCo_2O_4$-R precursor was synthesized *via* a solvothermal method. Typically, 0.4201 g $NiSO_4{\cdot}7H_2O$, 0.7318 g $CoCl_2{\cdot}6H_2O$ and 3.2432 g urea were dissolved in 60 mL of distilled water and ethylene glycol (1:2, v/v) and was poured into a Teflon-lined autoclave (100 mL) at 150 °C for 5.5 h. Then, the product was dried at 60 °C overnight.

$NiCo_2O_4$-N precursor was synthesized by a sol-gel method according to a previous research [33]. Typically, 2.4884 g $Ni(CH_3COO)_2{\cdot}4H_2O$, 4.9816 g $Co(CH_3COO)_2{\cdot}4H_2O$ and 12.61 g citric acid were dissolved in 250 mL pure $H_2O$ under vigorous stirring. The solution was then placed in an electrical oven at 120 °C for 8 h.

Finally, the three precursors were also calcined uniformly at 400 °C in air for 3 h with a ramping rate of 2 °C $min^{-1}$ to obtain corresponding morphology of $NiCo_2O_4$.

### 2.3. Characterization

Scanning electron microscopy (SEM) images were collected using a Hitachi SU8000 microscope (Japan). The BET surface areas were estimated from $N_2$ adsorption-desorption isotherms on a Micromeritics Tristar 3020 apparatus (Norcross, GA). The crystal structure and phase purity of 3D $NiCo_2O_4$-S were identified by a Bruker D8 X-ray diffractometer (XRD, Germany) with CuKα-radiation. The magnetic property of 3D $NiCo_2O_4$-S was evaluated by a Lakeshore 7407 vibrating sample magnetometer (VSM, USA). Thermogravimetric analysis (TGA) was carried out using a SDT Q600 thermoanalyzer at a ramping of 10 °C $min^{-1}$ with an air flow rate of 100 mL $min^{-1}$. The zeta potential of 3D $NiCo_2O_4$-S was taken with a Zetasizer Nano-ZS90 apparatus (Malvern, U.K.). UV–vis diffuse reflectance spectrum (DRS) was obtained by a UV2550 UV–vis spectrometer (Shimadzu, Japan) with $BaSO_4$ as the reflectance standard. FTIR spectra of 3D $NiCo_2O_4$-S were taken by Nicolet 5700 FTIR spectrophotometer. Mott-Schottky analysis was performed from −1.0 to 1.0 V in a conventional three-electrode configuration with fluorine-tin oxide (FTO) conducting glass (1cm × 1 cm) as working electrode (1 g $L^{-1}$ of 3D $NiCo_2O_4$-S sample suspension was dip-coated onto the conductive FTO glass), Pt wire as auxiliary electrode and a commercial Ag/AgCl as reference electrode on a CHI 660D workstation (Shanghai Chenhua, China). $Na_2SO_4$ aqueous solution (0.5 mol $L^{-1}$) was employed as electrolyte.

### 2.4. Experimental procedure

The degradation experiments were conducted in a temperature-controllable XH100B MW oven with a reflux condenser (Beijing XiangHu Ltd., China). If no specific instructions are given, the power and temperature of the oven were set to 700 W and 100 °C, respectively. Typically, prior to MW irradiation, 10 mg $NiCo_2O_4$ sample was introduced into a 250 mL three-necked flask containing 50 mL CR solution (20 mg $L^{-1}$). 3 mL of sample was withdrawn and separated magnetically to remove $NiCo_2O_4$ before analysis. For comparison, the experiments were also conducted without any catalyst under MW irradiation and with $NiCo_2O_4$ catalyst in the absence of MW irradiation.

### 2.5. Analytical methods

The spectra of CR solution after treatment were obtained by a UV–vis spectrometer. HPLC (Agilent 1100, USA) with a Zorbax Extend SB-C18 reverse-phase HPLC column (150 × 4.6 mm, 5 μm), a column oven and a diode array detector (DAD) was employed to detect the residual CR concentration in aqueous solution. The injection volume was 20 μL. The mobile phase was acetonitrile–50 mM NaAc containing 10 mM TBAB buffer solutions at pH 4.5 (50:50, v/v) with a flow rate of 1.0 mL $min^{-1}$ at 30 °C.

Further, to determine the reaction products (such as $NO_3^-$ and $SO_4^{2-}$) of CR after MW irradiation, a Dionex ICS-90 IC (USA) equipped with an IonPac AS9-HC column (250 × 4.0 mm) and a conductivity detector was utilized. The eluent phase was 9.0 mmol $L^{-1}$ $Na_2CO_3$ with a flow rate of 1.0 mL $min^{-1}$. The injection volume was 10 μL.

Surface charge property of 3D $NiCo_2O_4$-S was evaluated according to the previous report [34]. Typically, 10 mg of 3D $NiCo_2O_4$-S power was introduced into 100 mL of 0.003 mol $L^{-1}$ KCl solution. The initial pH value of the solution was adjusted from 4.0 to 13.0 with 0.01 mol $L^{-1}$ $HNO_3$ or KOH. The zeta potentials of samples were measured using a Zeta potential analyzer (Malvern, U.K.). The point of zero charge pH ($pH_{pzc}$) is the pH value of solution when the net charge on the surface of a sample is zero.

The formation of hydroxyl radicals (•OH) in the MICD process was identified through the photoluminescence (PL) probing technique via reacting TA with •OH to form highly fluorescent 2-hydroxyterephthalic acid [35,36]. The PL intensity at 425 nm was in proportion to the amount of •OH generated in water. The process was similar to that of catalytic degradation of CR, with CR solution replaced by TA–NaOH solution.

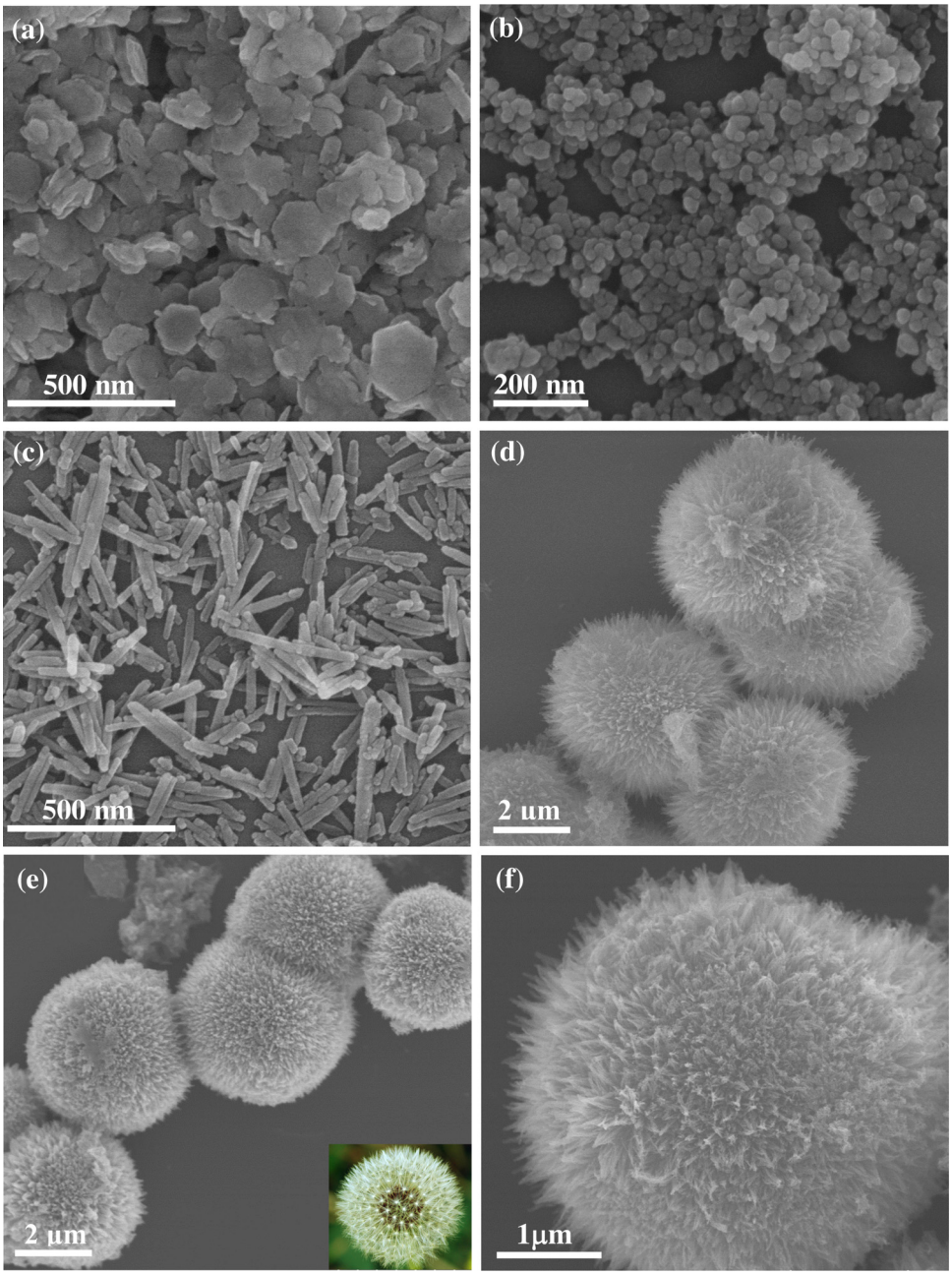


**Fig. 1.** SEM images of $NiCo_2O_4$-P (a), $NiCo_2O_4$-N (b), $NiCo_2O_4$-R(c), 3D $NiCo_2O_4$-S precursor (d) and 3D $NiCo_2O_4$-S (e and f).

## 3. Results and discussion

### 3.1. Characterization of $NiCo_2O_4$

Fig. 1 shows the representative SEM images of $NiCo_2O_4$-P, $NiCo_2O_4$-N, $NiCo_2O_4$-R, 3D $NiCo_2O_4$-S precursor and 3D $NiCo_2O_4$-S, respectively. Fig. 1**a** illustrates the SEM micrograph of the $NiCo_2O_4$-P, showing the hexagonal nanoplates with diameters of about 100 nm. Fig. 1**b** displays the SEM image of the $NiCo_2O_4$-N, showing the irregular spherical formation of 30–50 nm in diameter. The agglomeration of the $NiCo_2O_4$-P and $NiCo_2O_4$-N was also observed due to their magnetic interactions and high surface energy, which will affect their catalytic activity. The morphology of the $NiCo_2O_4$-R was also observed by SEM (Fig. 1**c**), which shows a nanorod structure with a diameter around 30 nm and a length extended to several hundred nanometers. It is clearly observed that the 3D $NiCo_2O_4$-S precursor exhibits obvious 3D dandelion-like structure with uniform diameters of 4 μm (Fig. 1**d**). After annealing, as shown in Fig. 1**e,** the morphologies of the 3D $NiCo_2O_4$-S do not change a lot, maintaining the hetero-architecture. The high-magnification SEM image (Fig. 1**f**) exhibits that the 3D $NiCo_2O_4$-S is actually constructed by numerous small secondary nanorods which grow along the radial direction. Based on the above observation, the 3D $NiCo_2O_4$-S may have an advantage in MICD process for CR, which was attributed to high MW energy harvesting capacity of the unique 3D porous hetero-architecture structure.

In order to explore suitable calcination temperature, the thermal behavior of the 3D $NiCo_2O_4$-S precursor in air is showed in TG/DTG curve (see Fig. 2a). The gradual weight loss (about 4.7%) at the temperature below 210 °C is due to the evaporation of physically adsorbed water and crystal water from metal salts. The main weight loss of 20.3% during 210–400 °C should be ascribed to the

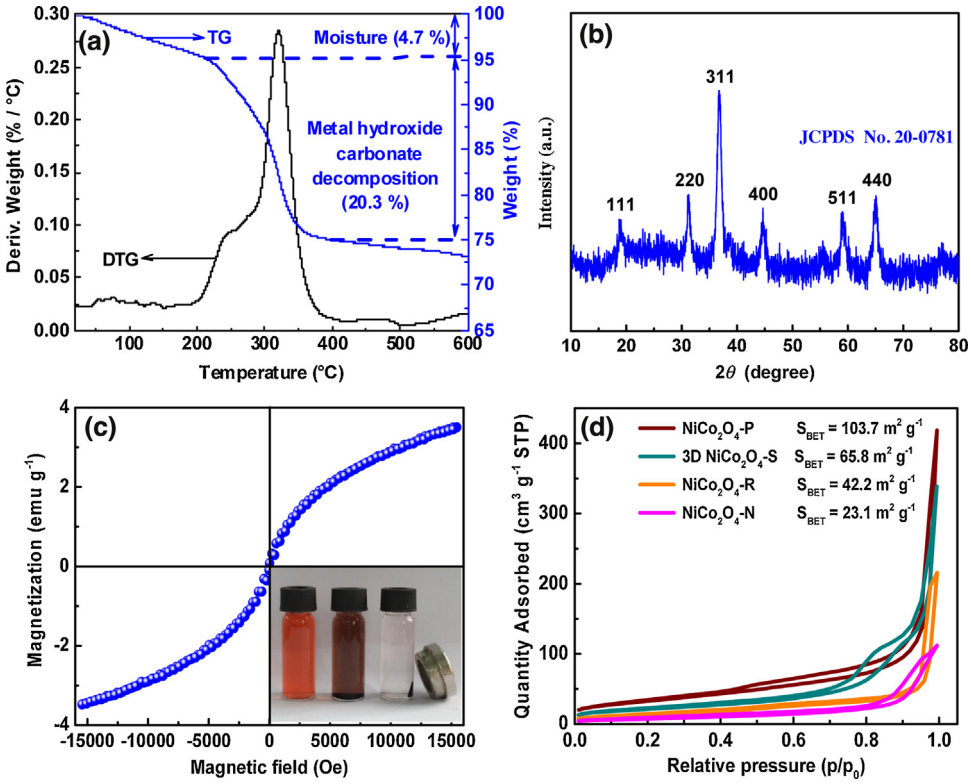


**Fig. 2.** TG/DTG curve (a), XRD spectrum (b) and Magnetic hysteresis loops (c) (inset: the photo of magnetic separation) of 3D $NiCo_2O_4$-S; $N_2$ adsorption–desorption isotherm of four kinds of $NiCo_2O_4$ samples (d).

decomposition of the Ni–Co hydroxide carbonate into $NiCo_2O_4$ in the presence of the air stream. No obvious weight loss over 400 °C is observed, indicating that the precursor has turned into $NiCo_2O_4$ completely at the temperature higher than 400 °C. In order to completely decompose the precursor to obtain phase pure $NiCo_2O_4$ oxides, a temperature of 400 °C is employed in the annealing process.

Fig. 2**b** shows the XRD pattern of the prepared 3D $NiCo_2O_4$-S. The diffraction peaks at 2$\theta$ values of 18.9°, 31.2°, 36.7°, 44.6°, 59.1° and 65.0° match well with the (111), (220), (311), (400), (511) and (440) crystal planes of $NiCo_2O_4$ with a cubic spinel structure (JCPDS No. 20-0781), indicating the successful synthesis of $NiCo_2O_4$ [37]. Besides, no peak from other crystallized phases can be detected, demonstrating the high purity of the 3D $NiCo_2O_4$-S.

Fig. 2**c** represents the field-dependent magnetic behavior of the 3D $NiCo_2O_4$-S, measured under an applied field of ±16.0 kOe at room temperature (inset: the photo of magnetic separation). It is seen that complete saturation is not achievable even in fields as high as 16.0 kOe, and a low coercive field of 80.1 Oe is observed, demonstrating the 3D $NiCo_2O_4$-S is a type of soft magnetic material. The considerable value of magnetization is 3.5 emu $g^{-1}$ at 16.0 kOe, which can make 3D $NiCo_2O_4$-S easily separated from the aqueous dispersion after their uses by an external magnetic field.

Generally, the BET surface area is an essential factor of the catalysts, which can markedly influence their catalytic activity. Hence, the BET surface areas of $NiCo_2O_4$-P, $NiCo_2O_4$-R, $NiCo_2O_4$-N and 3D $NiCo_2O_4$-S were estimated by $N_2$ adsorption/desorption isotherms to be 103.7, 42.2, 23.1 and 65.8 $m^2$ $g^{-1}$, respectively (Fig. 2**d**).

### 3.2. Microwave-induced catalytic activity of the catalysts

Microwave-induced catalytic activity of $NiCo_2O_4$-P, 3D $NiCo_2O_4$-S, $NiCo_2O_4$-R and $NiCo_2O_4$-N were estimated by degradation for a target dye-CR, a conventional environmental contaminant from industry wastewater. The degradation of CR has been often used as a model reaction to evaluate the performance of various methods [38–40].

Initially, experiments were performed in the absence of either as-prepared $NiCo_2O_4$ or MW as comparisons. Then, the MICD of CR over as-prepared $NiCo_2O_4$ was conducted under MW irradiation. Fig. 3**a** shows the removal efficiency of different $NiCo_2O_4$ samples by adsorption or catalysis. The removal efficiencies of CR were only about 10.1%, 43.0%, 13.6% and 7.4% after 10 min over $NiCo_2O_4$-P, 3D $NiCo_2O_4$-S, $NiCo_2O_4$-R and $NiCo_2O_4$-N in the absence of MW, respectively. It was also clearly revealed that self-degradation of CR without any catalyst under direct MW irradiation was almost negligible. However, all of the synthesized catalysts exhibited enhanced catalytic activities under MW irradiation. It is inferred that there is synergy effect of $NiCo_2O_4$ catalysts and MW irradiation.

Generally, the large BET surface area of the catalysts allows more surface to be reached by the incident MW and offers more reactive sites in MICD process. Fig. 3**a** shows that 3D $NiCo_2O_4$-S exhibits strong degradation ability towards CR. Around 90.1% of CR can be degraded by 3D $NiCo_2O_4$-S within 10.0 min, while $NiCo_2O_4$-P can only decompose less than 35.0% of CR. The microwave-induced degradation efficiency of $NiCo_2O_4$-P is lower than that of 3D $NiCo_2O_4$-S and $NiCo_2O_4$-R (53.5%), even though its BET surface area is larger than that of 3D $NiCo_2O_4$-S and $NiCo_2O_4$-R (see Fig. 2**d**), indicating that the BET surface area is not the only role in governing the catalytic activity.

Meanwhile, it is interesting to note that the morphology of $NiCo_2O_4$ samples dramatically affects the catalytic activities of $NiCo_2O_4$ catalysts under MW irradiation. The highest catalytic activity for the 3D $NiCo_2O_4$-S in comparison to other three $NiCo_2O_4$ samples may be due to its unique morphology with numerous secondary nanorods radially grown from their common centre, which allows multiple absorption and scattering of the incident MW, as shown in Scheme 1. The hierarchical morphology of 3D $NiCo_2O_4$-S

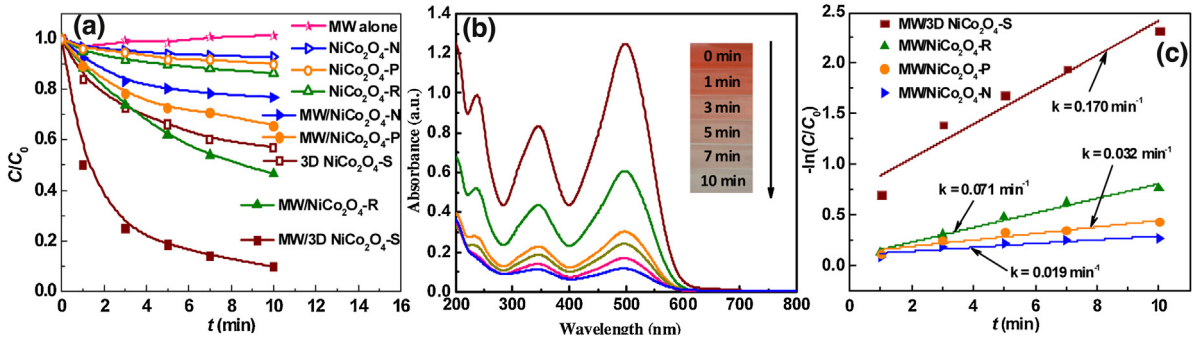


**Fig. 3.** (a) Removal efficiency of CR with different catalysts; (b) Absorption spectra of CR at different MW irradiation time in the presence of 3D $NiCo_2O_4$-S; (c) The kinetic curves. (20.0 mg $L^{-1}$ CR, natural pH 6.1, 0.2 g $L^{-1}$ catalyst in 50.0 mL solution, 700 W power).

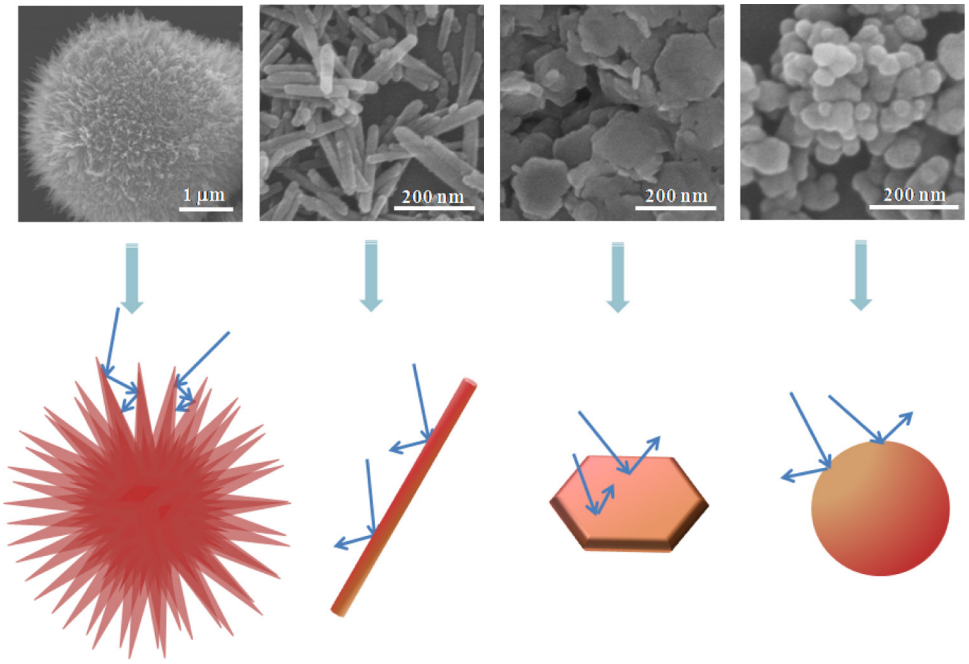


**Scheme 1.** Schematic illustration of multi-absorption within 3D $NiCo_2O_4$-S compared with $NiCo_2O_4$-R, $NiCo_2O_4$-P and $NiCo_2O_4$-N.

makes for the large BET surface area and high MW energy absorption capacity, which collectively result in the best MW catalytic performance.

Hence, we consider that the BET surface area, morphology and MW energy absorption ability of catalysts are three essential factors to obviously affect the catalytic activity in the MICD.

At the same time, Fig. 3**b** exhibits a gradual decrease of CR aqueous absorption at 497 nm under MW irradiation. Furthermore, no any new absorption bands appeared in the whole regions, further indicating the complete decolorization of CR during the MICD. The color change of CR solution from red to almost colorless in the photos (inset of Fig. 3**b**) also clearly revealed that the CR had been successfully degraded under MW/3D $NiCo_2O_4$-S. Hence, 3D $NiCo_2O_4$-S was selected as catalysts in this MICD system.

To understand the reaction kinetics of CR degradation further, the apparent pseudo first-order process expressed in the equation was used in the experiments.

$$-\ln\left(\frac{C}{C_0}\right) = kt + a \quad (1)$$

where $C_0$ is the initial CR concentration (mg $L^{-1}$), $C$ the concentration at time $t$ (min), and $k$ is the apparent first-order rate constant ($min^{-1}$). By using the first-order linear fit of the data from Fig. 3**c**, the $k$ value for 3D $NiCo_2O_4$-S, $NiCo_2O_4$-R, $NiCo_2O_4$-P and $NiCo_2O_4$-N were 0.170, 0.071, 0.032 and 0.019 $min^{-1}$, respectively. Obviously, the $k$ value of 3D $NiCo_2O_4$-S was approximately 2.39, 5.31 and 8.95 times higher than that of $NiCo_2O_4$-R, $NiCo_2O_4$-P and $NiCo_2O_4$-N, respectively, further suggesting the enhanced catalytic activity of the 3D $NiCo_2O_4$-S.

### 3.3. *Effects of pH*

The influence of initial pH values on the CR degradation were investigated in an initial pH range of 4–10. As presented in Fig. 4**a**, the constant color removal (approximately 90%) was observed in pH 4.0–7.0, and decreased slightly at higher pHs. Generally, the original pH of CR solution (20 mg $L^{-1}$) was about 6.1. Hence, these solutions were used directly without any pH adjustment in this work.

Generally, the solution pH influences adsorption behavior for organic dyes on the surface of catalyst. It is suggested that the surface of 3D $NiCo_2O_4$-S carries a net positive charge at pH $<pH_{pzc}$ ($pH_{pzc}$ = 11.2, Fig. 4**b**), while CR is negatively charged (inset, Fig. 4**a**). Additionally, only the CR molecules that have been adsorbed on the surface of catalyst can be degraded successfully. Therefore, the

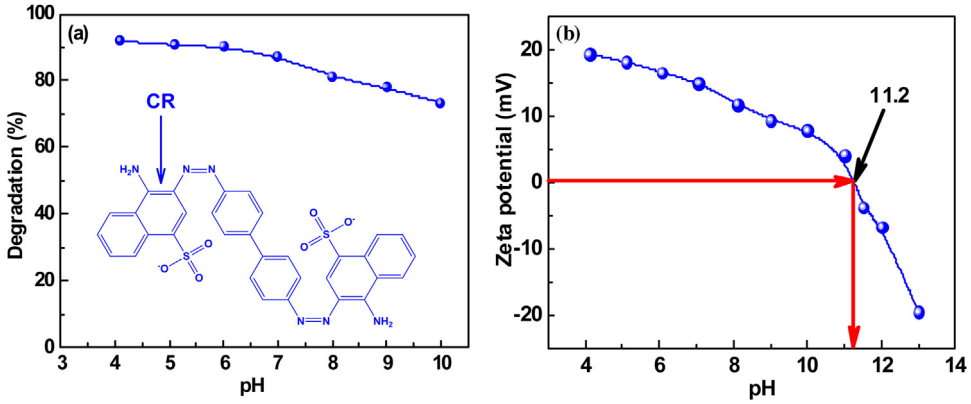


**Fig. 4.** (a) The effect of initial pH on the degradation of CR (20.0 mg $L^{-1}$ CR, 0.2 g $L^{-1}$ 3D $NiCo_2O_4$-S in 50.0 mL solution, 700 W power, MW irradiation for 10 min); (b) Zeta potential of 3D $NiCo_2O_4$-S at different pHs.

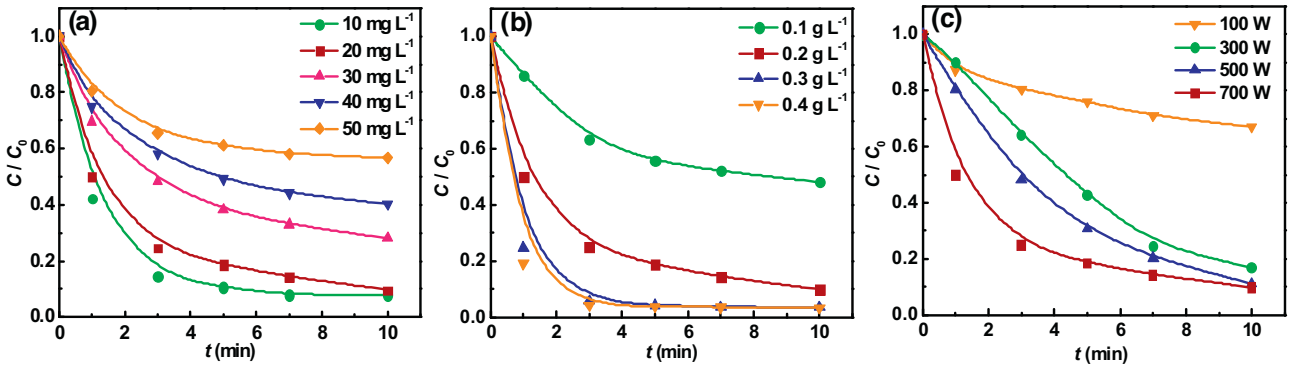


**Fig. 5.** (a) The effect of the initial concentration (natural pH 6.1, 0.2 g $L^{-1}$ 3D $NiCo_2O_4$-S in 50.0 mL solution, 700 W power), (b) The effect of 3D $NiCo_2O_4$-S dosage on the degradation of CR. (20.0 mg $L^{-1}$ CR, natural pH 6.1, 700 W power) and (c) The influence of MW power on the degradation of CR. (20.0 mg $L^{-1}$ CR, natural pH 6.1, 0.2 g $L^{-1}$ 3D $NiCo_2O_4$-S in 50.0 mL solution).

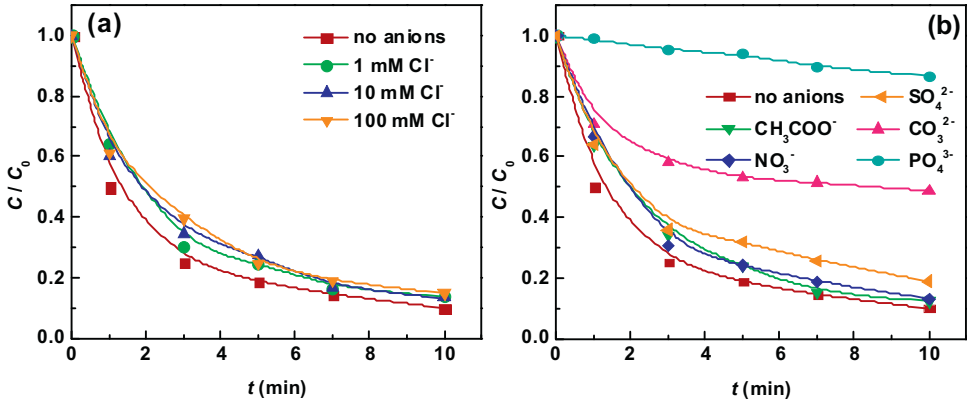


**Fig. 6.** (a) Influence of $Cl^-$ concentrations on the degradation of CR and (b) Degradation of CR in the presence of different anions. (20.0 mg $L^{-1}$ CR, natural pH 6.1, 0.2 g $L^{-1}$ 3D $NiCo_2O_4$-S in 50.0 mL solution, 700 W power).

low pH value can improve CR adsorption due to the electrostatic attraction and further promote better catalytic degradation.

### 3.4. Effect of initial CR concentration, 3D $NiCo_2O_4$-S dose and MW power

Initial concentration of the dye solution is an important factor for practical applications. The influence of initial dye concentration on the degradation was estimated in ranges from 10 to 50 mg $L^{-1}$. At presented in Fig. 5**a**, the degradation efficiency of CR under MW irradiation for 10 min gradually decrease with increasing CR concentration, while it maintain above 90% at 20 mg $L^{-1}$. A possible reason is that more organic substances are adsorbed on the surface of 3D $NiCo_2O_4$-S with the increasing CR initial concentration, but the MW irradiation time and active sites of catalyst are constant.

Usually, catalyst dosage is a key factor for catalytic degradation in treating environmental wastewater. The experiments were carried out to observe the CR degradation efficiencies with different catalyst dosage in the range of 0.1–0.4 g $L^{-1}$. As presented in Fig. 5**b**, the CR degradation efficiencies increase from 51.9% to 96.8% with increasing catalyst dosage. The larger catalyst dosage can increase the available catalyst surface area and thus the num-

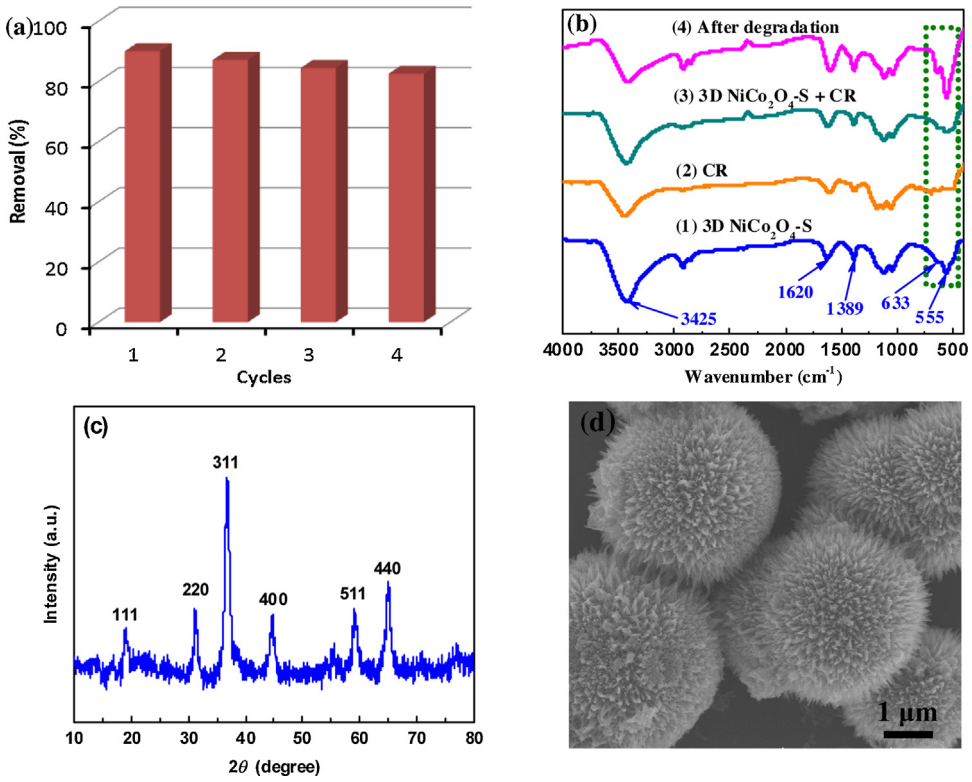


**Fig. 7.** (a) Cyclic tests of 3D $NiCo_2O_4$-S; (b) FTIR spectra of unused 3D $NiCo_2O_4$-S (1), CR (2), 3D $NiCo_2O_4$-S after CR adsorption (3) and 3D $NiCo_2O_4$-S after recycling four times (4); (c) XRD pattern after recycling four times; (d) SEM image after recycling four times. (20.0 mg $L^{-1}$ CR, natural pH 6.1, 0.2 g $L^{-1}$ 3D $NiCo_2O_4$-S in 50.0 mL solution, 700 W power, MW irradiation for 10 min).

ber of active sites, resulting the more generation of active species for the enhanced degradation of CR [41,42]. When the catalyst dosage was 0.2 g $L^{-1}$, more than 90% of CR was degraded after 10 min MW irradiation. Therefore, 0.2 g $L^{-1}$ of 3D $NiCo_2O_4$-S catalyst was used in our experiments.

It is generally known that MW output power is a crucial factor because it is the only energy source in MICD. As shown in Fig. 5**c**, under the same irradiation time, the color removal of the CR regularly enhanced with the increasing power from 100 to 700 W. More MW energy at higher power will form a lot of "hot spots" on the surface of 3D $NiCo_2O_4$-S and thus enhanced the generation of active species. Hence, considering degradation efficiency, the output power of 700 W was chosen in subsequent experiment.

### 3.5. Effect of electrolytes

The presence of inorganic anions, such as nitrate ($NO_3^-$), chloride ($Cl^-$), acetate ($CH_3COO^-$), carbonate ($CO_3^{2-}$), sulfate ($SO_4^{2-}$) and phosphate ($PO_4^{3-}$), is ubiquitous in real wastewater, especially in actual effluents from the dyestuff and textile industries [43]. The inorganic anions may have impacts on the performance of catalysis for the pollutants removal [44].

In this study, the influence of $Cl^-$ on the CR catalytic degradation in the MW/3D $NiCo_2O_4$-S system was investigated by adding NaCl into the CR solution prior to addition of 3D $NiCo_2O_4$-S at different $Cl^-$ concentrations of 0.001, 0.01 and 0.1 mol $L^{-1}$. As it was seen, while the CR degradation efficiency was achieved by 90.1% after MW irradiation for 10 min without additive, it was achieved by 86.4% at [$Cl^-$] = 0.001 mol $L^{-1}$, and no further decrease was achieved with an increased $Cl^-$ concentration up to 0.1 mol $L^{-1}$ (Fig. 6**a**). $Cl^-$ anion did show a negligible negative effect (approximately 3.7%) on the microwave-induced catalytic performance of 3D $NiCo_2O_4$-S in our case.

Fig. 6**b** shows the influences of different anions (i.e. $NO_3^-$, $CO_3^{2-}$, $CH_3COO^-$, $PO_4^{3-}$ and $SO_4^{2-}$) at the same 0.001 mol $L^{-1}$ of their sodium salts. To some extent, all anions discussed exhibited the inhibition effect for CR degradation. The inhibition degree of catalytic removal of CR caused by inorganic additives can be ranked in the following order: $PO_4^{3-} > CO_3^{2-} > SO_4^{2-} > NO_3^- \cong CH_3COO^- \cong Cl^-$. The side effect may be attributed to two reasons. It is reported that the inorganic anions may compete with organic solutes for the adsorption sites on the surface of catalyst [42,45], thereby causing a significant inhibition of catalytic efficiency. On the other hand, the inorganic anions as scavengers may also trap $h^+$ and $^{\bullet}OH$ [44,45], resulting in a decrease of the degradation efficiency.

### 3.6. Stability and reusability of 3D $NiCo_2O_4$-S

It is worth pointing out that the stability and reusability of the catalyst is crucial to practical application. The 3D $NiCo_2O_4$-S was recovered magnetically to perform multiple cycles of CR degradation. After each catalytic experiment, the catalyst was washed by ethanol/water (1:1, v/v) three times, dried at 60 °C for 12 h and activated at 400 °C in air atmosphere for 2 h. As shown in Fig. 7**a**, the decolorization ratios are 90.1% on the first run and 82.6% on the fourth run, which indicates that 3D $NiCo_2O_4$-S has a good reusability and stability in the MICD process.

In order to further testify the stability of 3D $NiCo_2O_4$-S, the FTIR and SEM analysis were carried out. It was observed that the FTIR spectra of 3D $NiCo_2O_4$-S after CR adsorption are clearly different from unused 3D $NiCo_2O_4$-S over a range of 400–800 $cm^{-1}$ (Fig. 7**b**). However, the FTIR spectra of 3D $NiCo_2O_4$-S after recycling four times demonstrated almost the same characteristic absorption peaks (3425, 1389, 1620, 633 and 555 $cm^{-1}$) as that of the unused 3D $NiCo_2O_4$-S (Fig. 7**b**). The XRD patterns after recycling four times (see Fig. 7**c**) indicated no obvious changes of the crystal structure

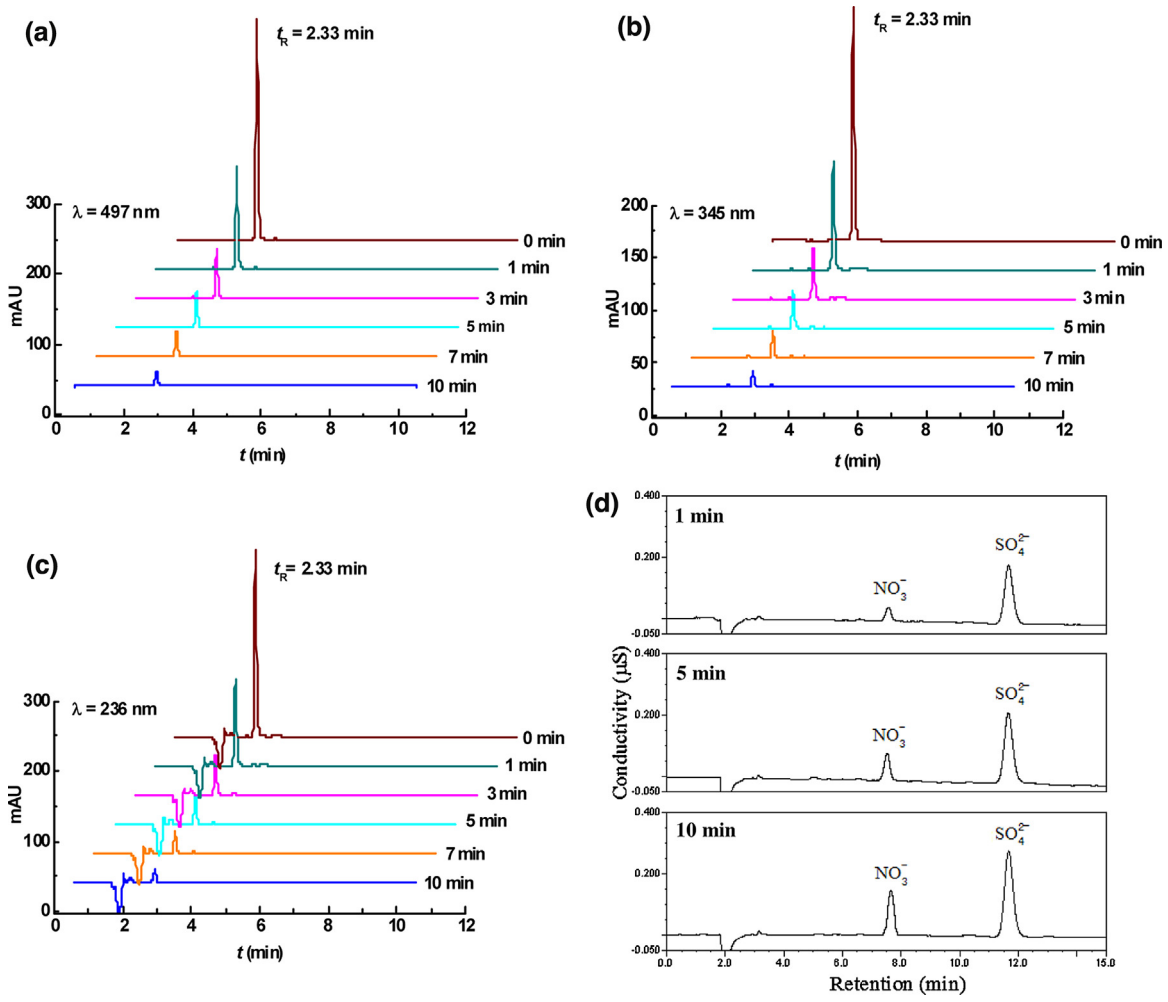


**Fig. 8.** HPLC chromatograms changes of CR over 3D $NiCo_2O_4$-S with detection wavelength as 497 nm (a), 345 nm (b) and 236 nm (c); IC chromatograms of CR solutions with different MW irradiation time (d). (20.0 mg $L^{-1}$ CR, natural pH 6.1, 0.2 g $L^{-1}$ 3D $NiCo_2O_4$-S in 50.0 mL solution, 700 W power).

over this catalyst during the degradation reaction. Moreover, the SEM image after recycling four times also did not change significantly (Fig. 7**d**). Therefore, the results of the acceptable activity in repeated uses and good stability showed that the 3D $NiCo_2O_4$-S synthesized by this simple method was promising in the practical application in wastewater treatment.

### 3.7. Identification of the intermediates and final products

To identify the degradation extent and degradation products, the HPLC analysis was performed at 497, 345 and 236 nm, respectively. As presented in Fig. 8**a–c**, the absorption maximum peak of CR appeared at $t_R$ = 2.33 min, and it decreased gradually with the increasing MW irradiation time, suggesting CR was degraded rapidly. Moreover, no new peak appeared, demonstrating no byproducts were identified.

To further validate degradation extent of CR, the IC was employed. Since CR molecule contains sulfur and nitrogen atoms, the $SO_4^{2-}$ and $NO_3^-$ ions should be potential degradation byproducts. It can be observed in Fig. 8**d** that two obvious peaks belonging to $NO_3^-$ and $SO_4^{2-}$ appear at retention time of 7.5 and 11.7 min, respectively. The IC peaks corresponding to $NO_3^-$ and $SO_4^{2-}$ gradually increased with irradiation time, proving that the C—N, C—S and N=N in the CR molecule were rapidly broken. That meant the nitrogen and sulfur atoms were oxidized and transformed into $NO_3^-$ and $SO_4^{2-}$ anions, respectively. Ultimately, CR was mineralized to a series of harmless inorganic ions (such as $CO_2$, $H_2O$, $NO_3^-$ and $SO_4^{2-}$).

### 3.8. Possible mechanism on the catalytic degradation

It has been widely acknowledged that •OH, hole ($h^+$) and superoxide radical ($^\bullet O_2^-$) are the active species for the MW catalytic oxidation [46]. To elucidate the microwave-induced catalytic mechanism of synthesized 3D $NiCo_2O_4$-S, the main active species were firstly detected through trapping experiments, as shown in Fig. 9**a**. In terms of $^\bullet O_2^-$, it can be observed that $N_2$ or air bubbling ($O_2$ is an electron-capturer to produce $^\bullet O_2^-$ [47].) has a negligible effect on the CR degradation, indicating that $^\bullet O_2^-$ on the surface of the 3D $NiCo_2O_4$-S is not the active species in the MW/3D $NiCo_2O_4$-S system. However, the catalytic activity of 3D $NiCo_2O_4$-S can be greatly suppressed by the addition of the $h^+$ scavenger (EDTA-2Na [48] or $Na_2C_2O_4$ [49], 1 mM), suggesting that the microwave-induced $h^+$ is the dominant oxidative species in this system. It can also be observed that TBA (7.9 wt.%, •OH scavenger [50]) or $NaHCO_3$ (1 mM, •OH scavenger [51]) has certain influence on the CR degradation, implying that •OH on the surface of the 3D $NiCo_2O_4$-S is also one of the oxidative species in the catalytic system. To summarize, the main reactive species in the MICD of CR are $h^+$ and •OH.

To further verify the participation of •OH in the degradation process, the PL spectroscopy using TA as a probe was employed

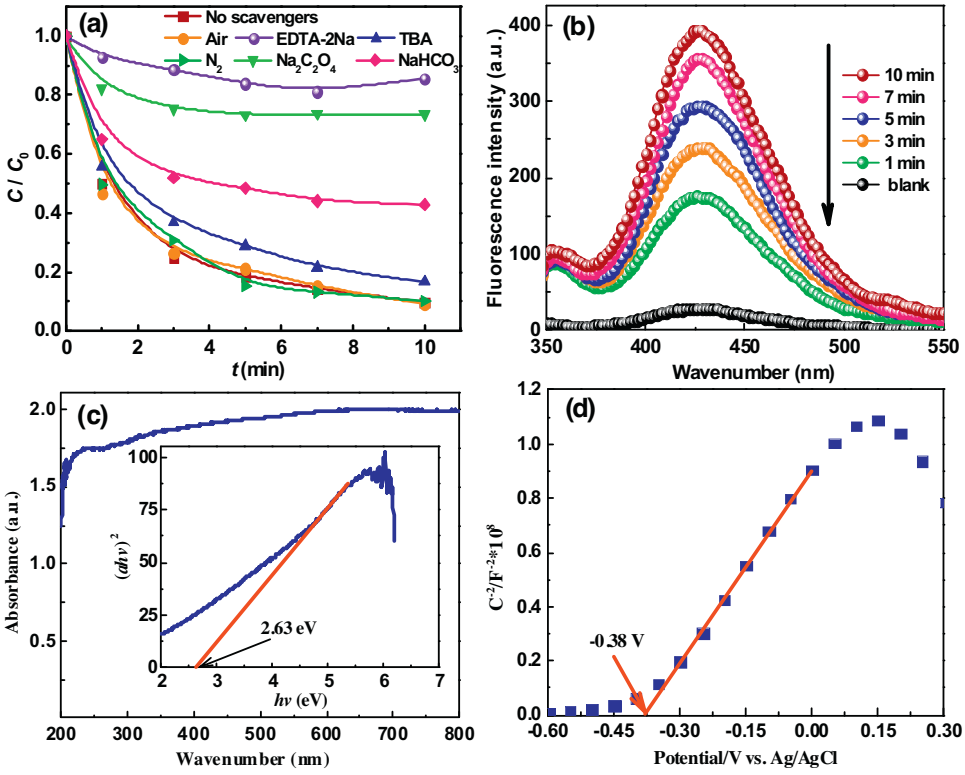


**Fig. 9.** (a) The effects of various scavengers on the degradation of CR over 3D $NiCo_2O_4$-S. (b) PL spectra at different MW irradiation time on 3D $NiCo_2O_4$-S in a $3 \times 10^{-4}$ mol $L^{-1}$ basic solution of TA. (c) DRS of 3D $NiCo_2O_4$-S (inset: plot of transformed Kubelka–Munk function versus the energy of light). (d) Mott–Schotty plots of 3D $NiCo_2O_4$-S.

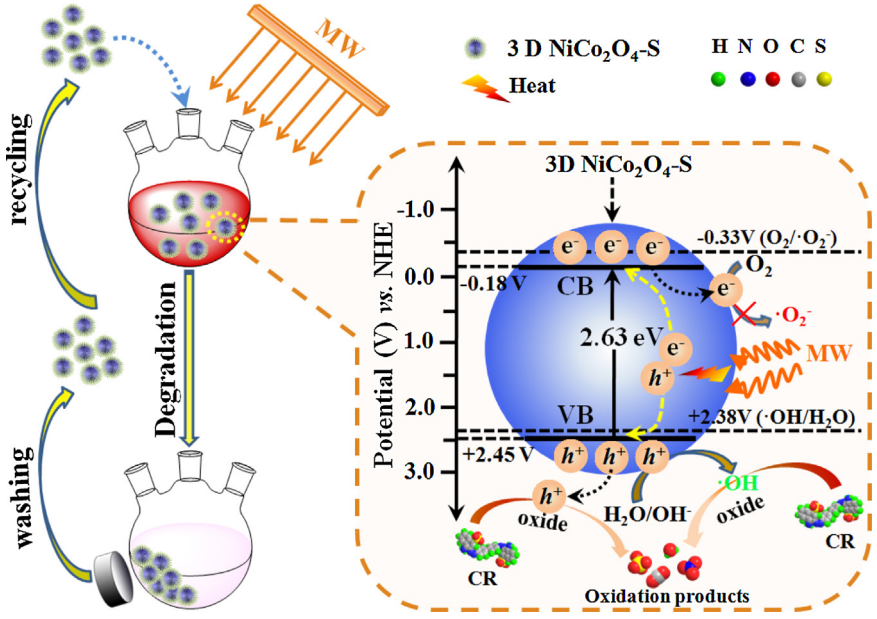


**Scheme 2.** Possible mechanism for 3D $NiCo_2O_4$-S under MW irradiation.

to determine the generated •OH in the MICD process. Fig. 9**b** exhibits the PL spectral changes from $3 \times 10^{-4}$ mol $L^{-1}$ TA solution in $2 \times 10^{-4}$ mol $L^{-1}$ NaOH with MW irradiation time. The PL intensity at 425 nm gradually increased along with irradiation time, demonstrating the formation of •OH.

In order to explain the enhanced microwave-induced catalytic activity, the DRS (Fig. 9**c**) and the flat-band positions ($V_{fb}$) (Fig. 9**d**) of the 3D $NiCo_2O_4$-S were measured. The band gap ($E_g$) of the 3D $NiCo_2O_4$-S was estimated to be 2.63 eV (inset, Fig. 9**c**). The $V_{fb}$ value can be determined to be roughly −0.38 V versus Ag/AgCl (equivalent to −0.18 V *vs.* NHE) according to the Mott-Schottky equation (Fig. 9**d**). Therefore, the conduction band potential ($E_{CB}$) is approximately −0.18 V. Furthermore, the value band potential ($E_{VB}$) is inferred to be about 2.45 V vs. NHE according to the $E_g$ value. The microwave-induced electrons ($e^-$) accumulated on the conduction band (CB) of the 3D $NiCo_2O_4$-S cannot reduce $O_2$ to yield $^{\bullet}O_2^-$, since the CB edge potential (−0.18 V vs. NHE) was more positive than the standard redox potential $E^{\theta}$ ($O_2/^{\bullet}O_2^-$) (-0.33 V vs. NHE)

[52,53]. This explains why $^{\bullet}O_2^-$ didn't participate in the MICD reaction. However, in view of the VB edge potential (2.45 V vs. NHE) is more positive than $E^{\theta}$ ($^{\bullet}OH/H_2O$) (2.38 V vs. NHE) [52,53], the MW generated $h^+$ left behind in the VB of the 3D $NiCo_2O_4$-S can theoretically oxidize $H_2O$ or hydroxyl group to form $^{\bullet}OH$, which was a very strong oxidant. Moreover, the $h^+$ could directly oxidize CR to harmless products. Therefore, the microwave-induced catalytic activity is significantly promoted, and CR is catalytically degraded through the $^{\bullet}OH$ or direct $h^+$ oxidation pathway.

Based on above experimental results and theoretical analysis, a plausible catalytic mechanism for CR in MW/3D $NiCo_2O_4$-S system was recommended, as illustrated in Scheme 2. The 3D $NiCo_2O_4$-S as MW absorber can intensively absorb and transfer MW energy, resulting in the production of "hot spots" (temperature >1473 K) on the surface of the 3D $NiCo_2O_4$-S. Under the MW excitation, the $e^-$ in 3D $NiCo_2O_4$-S could oscillate. Meanwhile, high heat from the "hot spots" could accelerate the movement of $e^-$ in 3D $NiCo_2O_4$-S and thereby induce the separation of $e^-/h^+$ pairs through thermal excitation. The heat-excited $e^-$ was migrated from the VB to the CB, leaving the $h^+$ on the VB of 3D $NiCo_2O_4$-S under MW irradiation. The leftover $h^+$ interacted with $H_2O$ or hydroxyl group on surface of 3D $NiCo_2O_4$-S to generate the $^{\bullet}OH$ which could efficiently degrade CR into $NO_3^-$, $SO_4^{2-}$, $CO_2$ and $H_2O$ et al. Simultaneously, the generated $h^+$ of 3D $NiCo_2O_4$-S is capable of oxidizing CR directly. The above process can be summarized by the following multi-stage reaction Eqs. (2)–(7):

$$\text{MW irradiation}(\text{“hot spot”effect}) \rightarrow \text{high heat} \quad (2)$$

$$[NiCo_2O_4] + \text{high heat} \rightarrow [NiCo_2O_4{}^*] \quad (3)$$

$$[NiCo_2O_4{}^*] \rightarrow [NiCo_2O_4] + h^+ + e^- \quad (4)$$

$$h^+ + H_2O(\text{surface}) \rightarrow {}^{\bullet}OH + H^+ \quad (5)$$

$$h^+ + OH^-(\text{surface}) \rightarrow {}^{\bullet}OH \quad (6)$$

$$\text{CR dye} + {}^{\bullet}OH + h^+ \rightarrow \text{oxidation products}(NO_3^-, SO_4^{2-}, CO_2 \text{ and } H_2O) \quad (7)$$

## 4. Conclusions

In this work, four different morphology of $NiCo_2O_4$, including $NiCo_2O_4$-P, $NiCo_2O_4$-R, $NiCo_2O_4$-N and 3D $NiCo_2O_4$-S, were successfully fabricated to explore the effects of their morphologies on the microwave-induced catalytic activity. Among them, the 3D $NiCo_2O_4$-S consisting of numerous small nanorods radially grown from their common centre exhibited the highest degradation efficiency, which can degrade 90.1% of CR during only 10 min. The large BET surface and efficient MW energy utilization synergistically contribute to the best degradation activity of 3D $NiCo_2O_4$-S. The 3D $NiCo_2O_4$-S may be a promising efficient catalyst to eliminate organic contaminants owing to its facile preparation strategy, recyclable magnetic separation and super-catalytic performance under MW irradiation.

## Acknowledgements

This work was financially supported by the National Nature Science Foundation of China (NSFC51178212), the Foundation of 211 project for Innovative Talent Training of Liaoning University, "123" Project of China Environmental Protection Foundation (No. CEPF2014-123-1-1) and the training programs of innovation and entrepreneurship for undergraduates of Liaoning University (X201510140143).

## Appendix A. Supplementary data

Supplementary data associated with this article can be found, in the online version, at http://dx.doi.org/10.1016/j.apcatb.2016.01.005.

## References

[1] S. Sadri Moghaddam, M.R. Alavi Moghaddam, M. Arami, J. Hazard. Mater. 175 (2010) 651–657.
[2] M.-X. Zhu, L. Lee, H.-H. Wang, Z. Wang, J. Hazard. Mater. 149 (2007) 735–741.
[3] S. Raghu, C. Ahmed Basha, J. Hazard. Mater. 149 (2007) 324–330.
[4] F. Mushtaq, M. Guerrero, M.S. Sakar, M. Hoop, A.M. Lindo, J. Sort, X. Chen, B.J. Nelson, E. Pellicer, S. Pane, J. Mater. Chem. A 3 (2015) 23670–23676.
[5] M. Shanmugam, A. Alsalme, A. Alghamdi, R. Jayavel, ACS Appl. Mater. Interfaces 7 (2015) 14905–14911.
[6] T. Maneerung, J. Liew, Y. Dai, S. Kawi, C. Chong, C.-H. Wang, Bioresour. Technol. 200 (2016) 350–359.
[7] B. Acevedo, R.P. Rocha, M.F.R. Pereira, J.L. Figueiredo, C. Barriocanal, J. Colloid Interface Sci. 459 (2015) 189–198.
[8] J. Fan, X. Jiang, H. Min, D. Li, X. Ran, L. Zou, Y. Sun, W. Li, J. Yang, W. Teng, G. Li, D. Zhao, J. Mater. Chem. A 2 (2014) 10654–10661.
[9] E. Hu, H. Cheng, Water Res. 57 (2014) 8–19.
[10] A.K. Haritash, C.P. Kaushik, J. Hazard. Mater. 169 (2009) 1–15.
[11] J. Li, D.H.L. Ng, P. Song, Y. Song, C. Kong, S. Liu, Mater. Res. Bull. 64 (2015) 236–244.
[12] E. Hu, Y. Hu, H. Cheng, J. Hazard. Mater. 299 (2015) 444–452.
[13] A.Y. Atta, B.Y. Jibril, T.K. Al-Waheibi, Y.M. Al-Waheibi, Catal. Commun. 26 (2012) 112–116.
[14] N. Remya, J.-G. Lin, Desalin. Water Treat. 53 (2015) 1621–1631.
[15] L. Bo, X. Quan, S. Chen, H. Zhao, Y. Zhao, Water Res. 40 (2006) 3061–3068.
[16] L. Olmedo, P. Hourquebie, F. Jousse, Adv. Mater. 5 (1993) 373–377.
[17] A.B. Ahmed, B. Jibril, S. Danwittayakul, J. Dutta, Appl. Catal. B 156–157 (2014) 456–465.
[18] X. Wang, L. Mei, X. Xing, L. Liao, G. Lv, Z. Li, L. Wu, Appl. Catal. B 160–161 (2014) 211–216.
[19] W. Shi, X. Liu, T. Zhang, Q. Wang, L. Zhang, RSC Adv. 5 (2015) 51027–51034.
[20] T.-Y. Wei, C.-H. Chen, H.-C. Chien, S.-Y. Lu, C.-C. Hu, Adv. Mater. 22 (2010) 347–351.
[21] H. Wu, G. Wu, Y. Ren, L. Yang, L. Wang, X. Li, J. Mater. Chem. C 3 (2015) 7677–7690.
[22] Y. Chen, M. Zhuo, J. Deng, Z. Xu, Q. Li, T. Wang, J. Mater. Chem. A 2 (2014) 4449–4456.
[23] A.N. Naveen, S. Selladurai, Electrochim. Acta 173 (2015) 290–301.
[24] H. Alamri, N. Ballot, J. Long, Y. Guari, J. Larionova, K. Kleinke, H. Kleinke, E. Prouzet, Chem. Mater. 26 (2014) 875–885.
[25] S.G. Mohamed, Y.-Q. Tsai, C.-J. Chen, Y.-T. Tsai, T.-F. Hung, W.-S. Chang, R.-S. Liu, ACS Appl. Mater. Interfaces 7 (2015) 12038–12046.
[26] S. Liu, J. Wu, J. Zhou, G. Fang, S. Liang, Electrochim. Acta 176 (2015) 1–9.
[27] Y. Mo, Q. Ru, J. Chen, X. Song, L. Guo, S. Hu, S. Peng, J. Mater. Chem. A 3 (2015) 19765–19773.
[28] D.P. Dubal, P. Gomez-Romero, B.R. Sankapal, R. Holze, Nano Energy 11 (2015) 377–399.
[29] Nhi S. Nguyen, G., Das, Hyon H. Yoon, Biosens. Bioelectron. 77 (2016) 372-377.
[30] S.N. Kale, A.D. Jadhav, S. Verma, S.J. Koppikar, R. Kaul-Ghanekar, S.D. Dhole, S.B. Ogale, Nanomed. Nanotechnol. 8 (2012) 452–459.
[31] A.K. Mondal, D. Su, S. Chen, X. Xie, G. Wang, ACS Appl. Mater. Interfaces 6 (2014) 14827–14835.
[32] J. Pu, J. Wang, X. Jin, F. Cui, E. Sheng, Z. Wang, Electrochim. Acta 106 (2013) 226–234.
[33] Y.Q. Wu, X.Y. Chen, P.T. Ji, Q.Q. Zhou, Electrochim. Acta 56 (2011) 7517–7522.
[34] S. Ullah, E.P. Ferreira-Neto, A.A. Pasa, C.C.J. Alcântara, J.J.S. Acuña, S.A. Bilmes, M.L. Martínez Ricci, R. Landers, T.Z. Fermino, U.P. Rodrigues-Filho, Appl. Catal. B 179 (2015) 333–343.
[35] E.O. Oseghe, S. Maddila, P.G. Ndungu, S.B. Jonnalagadda, Appl. Catal. B 176–177 (2015) 288–297.
[36] W. Ragsdale, S. Gupta, K. Conard, S. Delacruz, V.R. Subramanian, Appl. Catal. B 180 (2016) 442–450.
[37] T.N. Lambert, J.A. Vigil, S.E. White, D.J. Davis, S.J. Limmer, P.D. Burton, E.N. Coker, T.E. Beechem, M.T. Brumbach, Chem. Commun. 51 (2015) 9511–9514.
[38] A.M.S. Solano, S. Garcia-Segura, C.A. Martínez-Huitle, E. Brillas, Appl. Catal. B 168–169 (2015) 559–571.
[39] E.S. Aazam, J. Alloys Compd. 644 (2015) 1–6.
[40] M.M. Khan, S.A. Ansari, M.E. Khan, M.O. Ansari, B.-K. Min, M.H. Cho, New J. Chem. 39 (2015) 2758–2766.
[41] C. Cai, Z. Zhang, J. Liu, N. Shan, H. Zhang, D.D. Dionysiou, Appl. Catal. B 182 (2016) 456–468.
[42] D. Kanakaraju, C.A. Motti, B.D. Glass, M. Oelgemöller, Chemosphere 139 (2015) 579–588.
[43] H.-F. Lai, C.-C. Chen, Y.-K. Chang, C.-S. Lu, R.-J. Wu, Sep. Purif. Technol. 122 (2014) 78–86.

[44] D.E. Santiago, J. Araña, O. González-Díaz, M.E. Alemán-Dominguez, A.C. Acosta-Dacal, C. Fernandez-Rodríguez, J. Pérez-Peña, J.M. Doña-Rodríguez, Appl. Catal. B 156–157 (2014) 284–292.
[45] H. Barndõk, D. Hermosilla, C. Han, D.D. Dionysiou, C. Negro, Á. Blanco, Appl. Catal. B 180 (2016) 44–52.
[46] Y. Chen, Z. Ai, L. Zhang, J. Hazard. Mater. 235–236 (2012) 92–100.
[47] W. Li, D. Li, J. Wang, Y. Shao, J. You, F. Teng, J. Mol. Catal. A: Chem. 380 (2013) 10–17.
[48] S. Rtimi, S. Giannakis, R. Sanjines, C. Pulgarin, M. Bensimon, J. Kiwi, Appl. Catal. B 182 (2016) 277–285.
[49] X. Ding, W. Ho, J. Shang, L. Zhang, Appl. Catal. B 182 (2016) 316–325.
[50] A. Ikhlaq, D.R. Brown, B. Kasprzyk-Hordern, Appl. Catal. B 165 (2015) 408–418.
[51] Y. Su, Z. Wu, Y. Wu, J. Yu, L. Sun, C. Lin, J. Mater. Chem. A 3 (2015) 8537–8544.
[52] M. Zhou, D. Han, X. Liu, C. Ma, H. Wang, Y. Tang, P. Huo, W. Shi, Y. Yan, J. Yang, Appl. Catal. B 172–173 (2015) 174–184.
[53] J. Ma, C. Wang, H. He, Appl. Catal. B 184 (2016) 28–34.